SCIENCE CHINA
Information Sciences

• RESEARCH PAPER •

October 2025, Vol. 68, Iss. 10, 202405:1–202405:10
https://doi.org/10.1007/s11432-025-4526-2

Wafer-scale fabrication of monolayer MoS_2 films for two-dimensional electronic devices via multitube atmospheric-pressure chemical vapor deposition

Zixuan CHENG[1,2], Dingyi YANG[1], Yong WANG[1,2*], Yizhang WU[3], Biao WU[1], Jiateng ZHANG[1], Huan LIU[1,2], Mingwen ZHANG[4], Xuetao GAN[4*], Yan LIU[1,2*], Yue HAO[1,2] & Genquan HAN[1,2]

[1]*Wide Bandgap Semiconductor Technology Disciplines State Key Laboratory, School of Microelectronics, Academy of Advanced Interdisciplinary Research, Xidian University, Xi'an 710071, China*
[2]*Emerging Device and Chip Laboratory, Hangzhou Institute of Technology, Xidian University, Hangzhou 311200, China*
[3]*Department of Applied Physical Sciences, The University of North Carolina at Chapel Hill, Chapel Hill NC 27514, USA*
[4]*Key Laboratory of Light Field Manipulation and Information Acquisition, Ministry of Industry and Information Technology, and Shaanxi Key Laboratory of Optical Information Technology, School of Physical Science and Technology, Northwestern Polytechnical University, Xi'an 710129, China*

Received 24 January 2025/Revised 27 April 2025/Accepted 23 July 2025/Published online 23 September 2025

Abstract Two-dimensional (2D) transition-metal dichalcogenides (TMDCs) have emerged as promising materials for extending Moore's law owing to their dangling bond-free surface, ultrathin structure, high mobility, and tunable bandgap similar to silicon. To achieve their large-scale integration, the batch-controllable fabrication of wafer-scale films suitable for industrial applications is crucial. To this end, we developed a cost-effective multitube atmospheric-pressure chemical vapor deposition setup for successfully fabricating high-quality wafer-scale monolayer MoS_2 films on sapphire substrates. Characterization results show that the monolayer MoS_2 films exhibit uniform physical dimensions, a high-quality crystal structure, and excellent nonlinear optical properties. Furthermore, we revealed the regulatory effects of carrier-gas flow and viscous flow behavior on crystal quality during the film growth process. Then, monolayer-MoS_2-based ferroelectric field-effect transistors were assembled, which exhibited an outstanding current modulation ratio exceeding 10^6 and reliable electrical characteristics. This study provides an efficient and convenient solution for advancing the standardization of 2D material research, laying the foundation for the fabrication of large-scale integrated circuits and flexible electronics based on MoS_2.

Keywords atmospheric pressure, chemical vapor deposition, wafer-scale MoS_2, second harmonic generation, FeFETs

Citation Cheng Z X, Yang D Y, Wang Y, et al. Wafer-scale fabrication of monolayer MoS_2 films for two-dimensional electronic devices via multitube atmospheric-pressure chemical vapor deposition. Sci China Inf Sci, 2025, 68(10): 202405, https://doi.org/10.1007/s11432-025-4526-2

1 Introduction

The advancement of the integrated circuit technology has reduced the size of process nodes to 2 nm, thereby approaching the physical limits of silicon used in transistors. Therefore, new materials and integration technologies must be developed to further enhance transistor density in integrated circuits [1–4]. Two-dimensional (2D) transition-metal dichalcogenides (TMDCs) have emerged as promising materials for extending Moore's law because they are ultrathin and have high mobility, no surface dangling bonds, and a tunable bandgap comparable to silicon [5–11]. A unique feature of TMDCs is that their physical and chemical characteristics are highly dependent on the number of layers used. Thus, their electrical and optoelectronic properties were tuned by modifying the layer thickness. These characteristics make TMDCs ideal for use in diodes, photodetectors, memory devices, humidity sensors, and supercapacitors [10, 12–16]. As the number of layers decreases from a few layers to a monolayer, TMDCs transition from indirect to direct bandgap semiconductors [17]. By precisely fabricating TMDCs with different thicknesses, their properties were tailored for various applications.

* Corresponding author (email: yongwang@xidian.edu.cn, xuetaogan@nwpu.edu.cn, xdliuyan@xidian.edu.cn)

Molybdenum disulfide (MoS_2) is the most extensively studied semiconductor material among TMDCs. Monolayer MoS_2 has a thickness of 0.6 nm and a bandgap of ∼1.9 eV, with excellent optoelectronic properties, extremely low off-state current, and a relatively low subthreshold swing. Thus, it is an ideal channel material for next-generation low-dimensional semiconductor devices. The batch-controllable preparation of wafer-scale films is essential to enable the large-scale integration of MoS_2, for which various methods have been proposed such as chemical vapor deposition (CVD) [18–22], metal-organic CVD (MOCVD) [23], and atomic layer deposition (ALD) [24, 25]. CVD stands out for its ability to produce high-quality wafer-scale monolayer MoS_2 films via a simple process and at a lower cost. However, wafer-scale MoS_2 films are typically fabricated via low-pressure CVD (LPCVD), which requires a vacuum system to maintain a low-pressure environment, thereby considerably increasing the equipment complexity. MoS_2 films were deposited on substrates via atmospheric-pressure CVD (APCVD). This approach uses simple equipment and incurs low costs, making it more suitable for large-scale industrial integration. Therefore, it is imperative to analyze the growth mechanism of wafer-scale MoS_2 grown via APCVD under different growth conditions.

In this study, we developed a multitube APCVD setup and used sulfur and MoO_3 powders as precursors to fabricate high-quality wafer-scale monolayer MoS_2 films on vertical sapphire substrates. The sizes of individual MoS_2 domains reached up to 164 μm, which were effectively controlled by adjusting the carrier-gas flow. Further, the effect of the viscous flow of the carrier gas inside the quartz tube on crystal quality was investigated using the Knudsen equation. Characterization results demonstrated that the APCVD method yielded high-quality wafer-scale monolayer MoS_2 films with excellent nonlinear optical properties. The application potential of 2D electronic devices was verified by assembling a ferroelectric field-effect transistor (FeFET) fabricated by growing monolayer MoS_2 films on a sapphire substrate. This device exhibited excellent nonvolatile memory characteristics, including a large memory window, outstanding current modulation ratio, and reliable electrical properties. This study provides an efficient and low-cost approach for fabricating large-scale high-quality-MoS_2-based integrated circuits and the standardization of 2D material research.

2 Results and discussion

The experimental configuration for wafer-scale MoS_2 synthesis is illustrated in Figure 1(a). The reaction mechanism between S and MoO_3 during MoS_2 CVD growth is illustrated in Figure 1(b) and described by the following three equations [26]:

$$7\mathrm{S(s)} + 2\mathrm{MoO_3(s)} \rightarrow 2\mathrm{MoS_2(s)} + 3\mathrm{SO_2(g)}, \tag{1}$$

$$\frac{1}{2}\mathrm{S(s)} + \mathrm{MoO_3(s)} \rightarrow \mathrm{MoO_2(s)} + \frac{1}{2}\mathrm{SO_2(g)}, \tag{2}$$

$$3\mathrm{S(s)} + \mathrm{MoO_2(s)} \rightarrow \mathrm{MoS_2(s)} + \mathrm{SO_2(g)}. \tag{3}$$

Eq. (1) shows that under sulfur-rich conditions, S reacts directly with MoO_3 to yield MoS_2, indicating complete MoO_3 sulfurization. In contrast, Eqs. (2) and (3) describe scenarios under sulfur-deficient conditions; in such conditions, S and MoO_3 first react to form MoO_2, which then reacts with additional S to produce MoS_2. As MoO_2 has a higher melting point and lower vapor pressure than MoO_3, sulfur-rich environments are more favorable for efficient MoS_2 synthesis. As shown in Figure S1, the sapphire substrate is vertically positioned within a hollow quartz holder facing the precursor source. This arrangement reduces distance-induced precursor concentration gradients, thereby enhancing uniformity and growth rate.

The monolayer MoS_2 synthesized by APCVD was characterized via optical microscopy and spectroscopy, confirming its high quality. Figure 1(d) displays the optical morphology of the 2-inch C-plane sapphire substrate coated with wafer-scale MoS_2, compared to a blank substrate. Figure S2 in the Supplementary Note 2 shows an optical microscope image of continuous monolayer molybdenum disulfide. Figure 1(c) shows an optical microscope image of the as-grown monolayer MoS_2, with a single crystal domain size of 100 μm and a maximum domain size of 164 μm. The AFM image in Figure 1(e) reveals a uniform surface with a thickness of 0.6 nm, indicating the monolayer MoS_2.

To evaluate the quality and uniformity of the as-grown MoS_2 monolayer films, Raman and photoluminescence (PL) measurements were performed at 17 evenly distributed locations across the 2-inch wafer, as indicated in Figure 2(a). The corresponding Raman and PL spectra are shown in Figures 2(b) and (c),

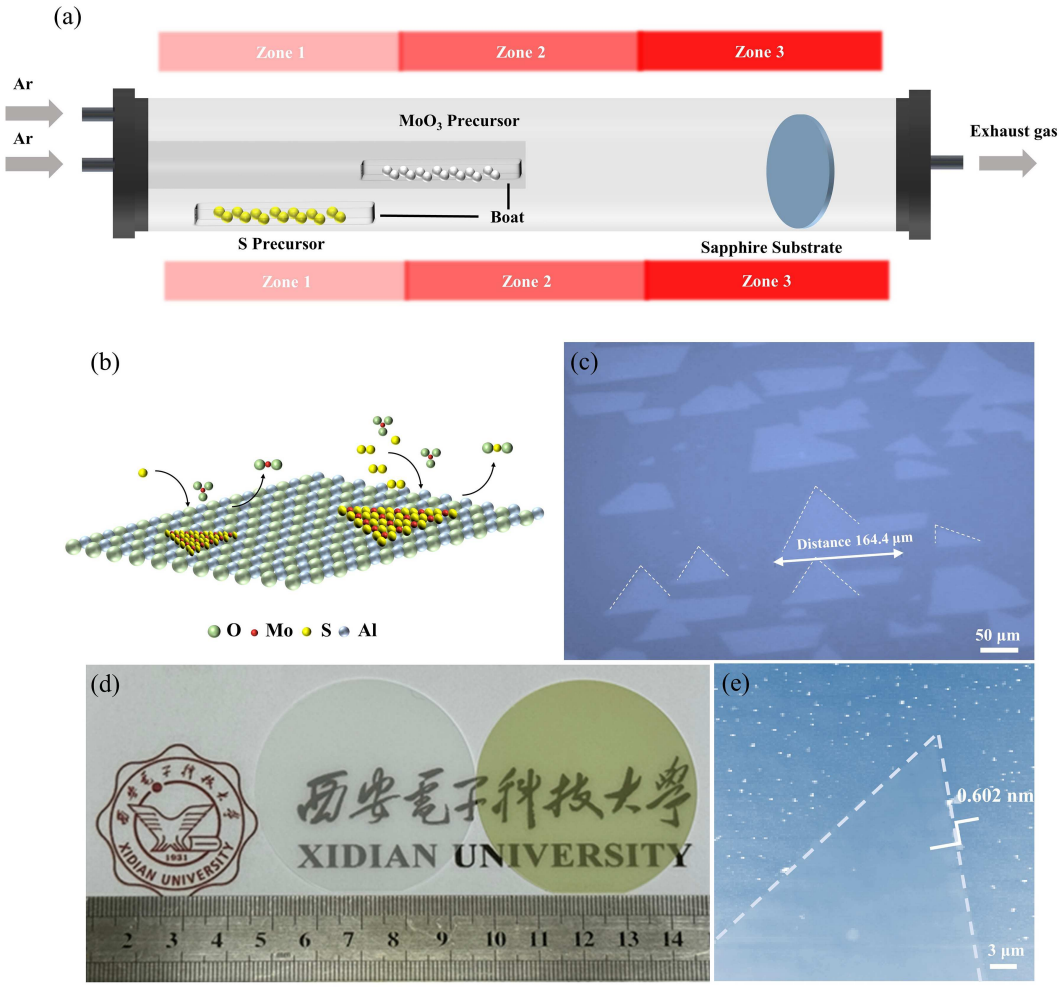

Figure 1 (Color online) (a) Schematic of the experimental setup for wafer-scale MoS_2 synthesis; (b) reaction mechanism for MoS_2 growth on sapphire substrate; (c) optical microscope image of large size monolayer MoS_2; (d) photographs of a 2-inch C-plane sapphire substrate (left) and a monolayer MoS_2 film on sapphire (right); (e) AFM image of the as-grown monolayer MoS_2.

respectively. Statistical histograms of the Raman peak separation and PL peak position (Figure 2(d)) exhibit narrow distributions, confirming the uniformity of the MoS_2 film across the wafer. In the Raman spectrum, the average peak difference between the E^1_{2g} and A_{1g} modes is approximately 20.1 cm^{-1}, a characteristic signature of monolayer MoS_2 [26–28]. A substrate-related Raman mode is also observed near 417.3 cm^{-1}, in the sapphire substrate (Figure S3). The PL spectra reveal a direct bandgap of approximately 1.86 eV for MoS_2, with an additional peak near 1.79 eV originating from the sapphire substrate (Figure S4). X-ray photoelectron spectroscopy (XPS) data, presented in Figures 2(e) and (f), display prominent peaks for MoS_2 at 232.7 eV (Mo $3d_{3/2}$), 229.6 eV (Mo $3d_{5/2}$) and 226.7 eV (S 2p), which confirms complete consumption of the molybdenum precursors and intermediate reactants [23, 29, 30]. Based on the above characterizations of monolayer MoS_2, it is demonstrated that the monolayer MoS_2 films prepared by APCVD exhibit high quality and uniformity.

Compared to conventional CVD operating under vacuum conditions, APCVD enables faster growth of large-area uniform 2D films. However, the higher flow dynamics of the carrier gas in APCVD necessitates precise control over flow rate and precursor concentration during the reaction to achieve high-quality films. Figure 3 presents optical images of MoS_2 films and statistical distributions of their grain sizes under varying gas flow rates. For each MoS_2 domain, the domain size was defined as the maximum edge length and quantified using ImageJ software. As shown in Figures 3(a) and (b), at a gas flow rate of 40 sccm, the average grain size of MoS_2 on the wafer is limited to 5 μm. This is because the slow carrier gas flow rate results in a significant insufficiency in the supply of the high-melting-point metal oxide precursor MoO_3, thereby hindering the progress of the target reaction. Increasing the gas flow rate to

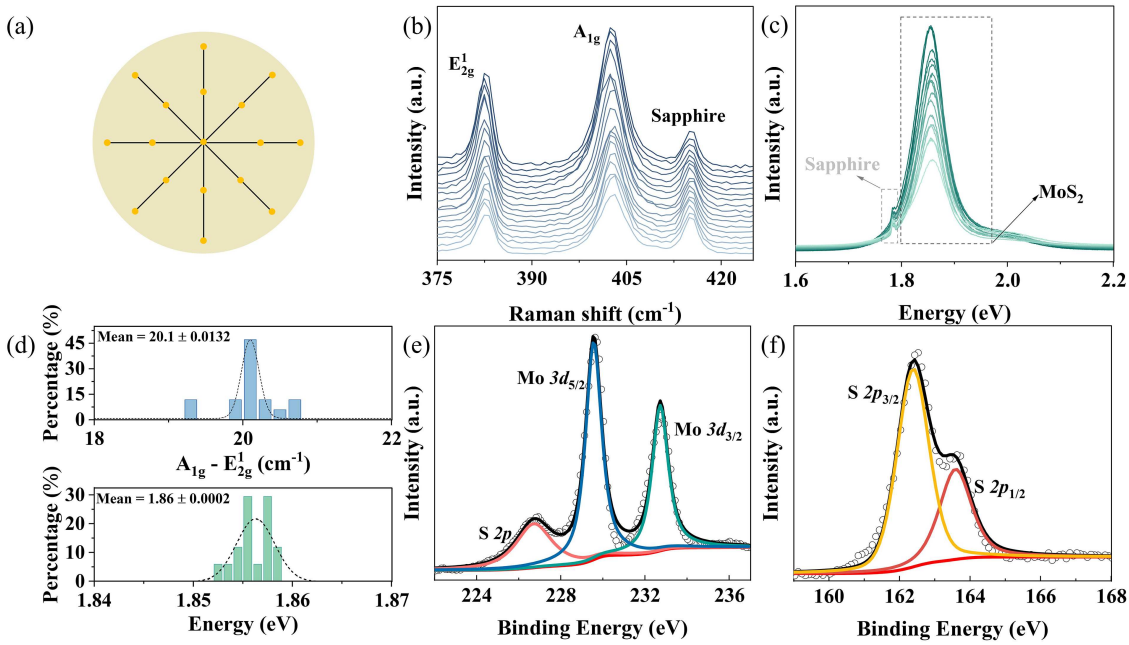

Figure 2 (Color online) (a) Schematic of 17 sampling locations on a 2-inch MoS_2/sapphire wafer; (b) Raman and (c) PL spectra at each sampling point; (d) histograms and Gaussian fits of Raman peak difference and PL peak position; XPS spectra of the synthesized monolayer MoS_2 film, showing (e) Mo and (f) S binding energies.

60 sccm (Figures 3(c) and (d)) yields grains with an average size of 70 μm and improved distribution uniformity. However, the grain density remains relatively low, indicating that nucleation is less frequent under these conditions. This phenomenon suggests that the supply of reactants is uniform and stable but not saturated, leading to lower nucleus formation while allowing the existing nucleus to grow into larger grains.

At 80 sccm, domain sizes at the wafer edge increase to 120 μm (Figures 3(e) and (f)), while central regions show marginal growth to 80 μm, likely due to precursor distribution asymmetry. As the gas flow rate further increases, the size of the MoS_2 domains exhibits a reduction phenomenon. Simultaneously, the gradually apparent difference emerges where the average grain size at the wafer edge becomes larger than that at the central region. At 140 sccm, the MoS_2 domains at the wafer center display a shift in morphology towards star-like triangles. This phenomenon can be attributed to a deficiency in Mo precursors and relatively high-density sulfur vapor, which induces rapid kinetically driven crystal growth [31–33]. These findings highlight APCVD's unique advantages in tuning domain size via gas flow rate, underscoring its process flexibility, and scalability in the controllable preparation of monolayer MoS_2.

The Knudsen number K_n during growth is defined as [34]

$$K_n = \frac{K_B T}{\sqrt{2}\pi d^2 p L}, \tag{4}$$

where K_B is the Boltzmann constant (1.380649×10^{-23} J/K); T is the temperature of the reaction system, set at 1203.15 K (930°C); d is the diameter of the gas molecules in the reactant vapor (nm scale); p is the pressure of the reaction system, set at 101 kPa during the growth process; and L is the distance from the closer MoO_3 precursor to the substrate, which is approximately 20 cm. During the MoS_2 reaction process, the K_n of all precursor molecules and carrier gas molecules remains below 0.1, indicating that gas flow within the quartz tube is viscous during the APCVD process. In this regime, gas molecules near the quartz tube wall experience a viscous drag force from the wall's resistance and decelerate, forming a boundary layer with reduced flow velocity. Frictional interactions between molecules in adjacent layers further contribute to a gradual velocity gradient, resulting in a characteristic parabolic flow profile. Consequently, gas flow velocity is highest at the center of the quartz tube. When the gas flow encounters the surface of the sapphire wafer, a stagnation point with near-zero velocity forms in the central region, while the flow spreads outwards. Moreover, the growth of MoS_2 occurs under sulfur-rich

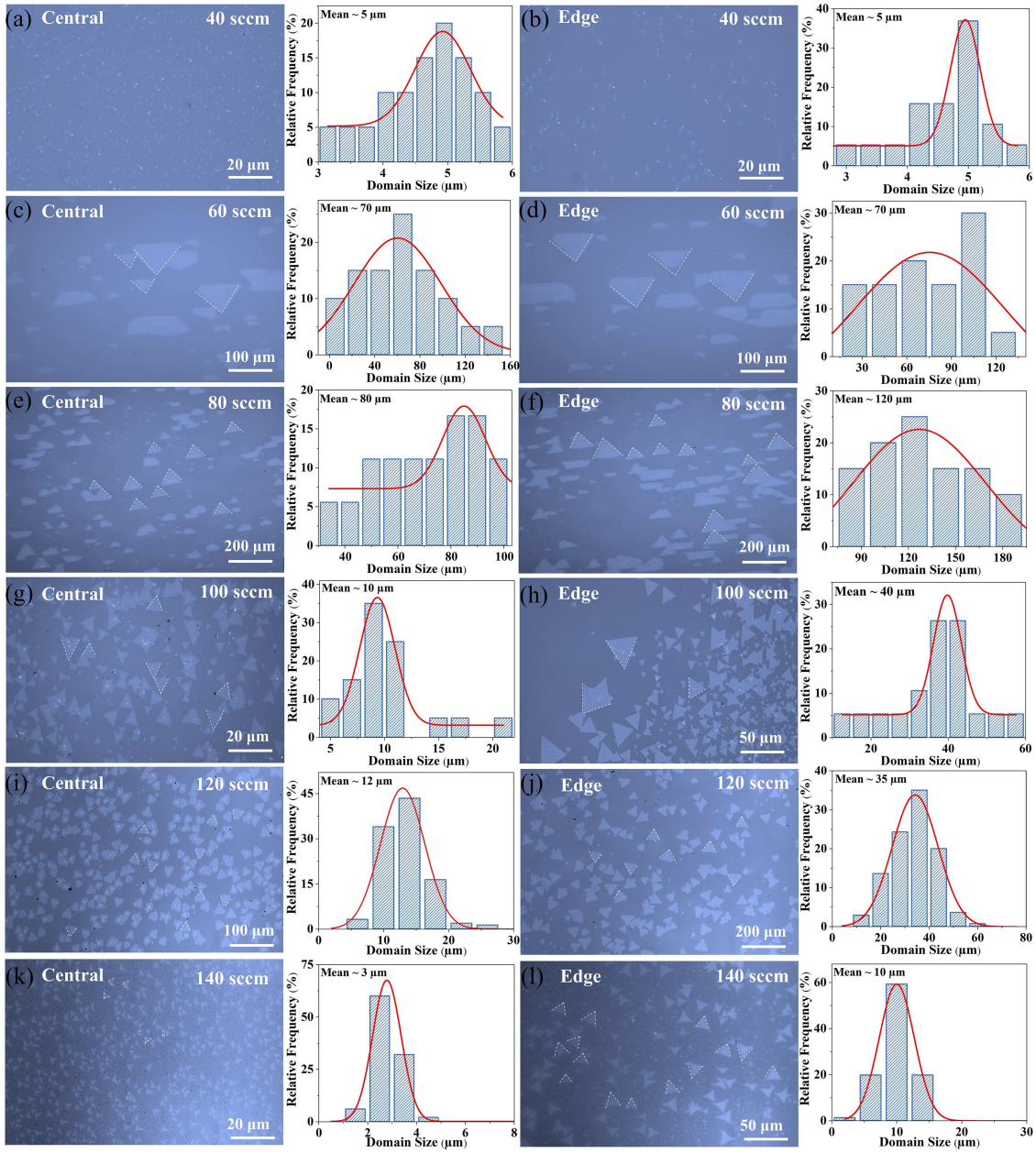

Figure 3 (Color online) Optical microscope images of monolayer MoS_2 domains at the center ((a), (c), (e), (g), (i), (k)) and edge ((b), (d), (f), (h), (j), (l)) of wafers for gas flow rates of 40–140 sccm in 20 sccm increments. Statistical plots of crystal domain size distribution are shown below each image pair.

conditions. Once a sufficient quantity of sulfur powder has vaporized, the sulfur concentration within the tube becomes relatively uniform, while the concentration distribution of Mo precursors is significantly influenced by viscous flow dynamics. Due to the parabolic velocity profile, the gas flow velocity at the wafer edges is higher than at the center, facilitating greater precursor transport to the edges. This results in the formation of much larger grains at the edges compared to the center.

At lower flow rates (<60 sccm), Mo precursor transport to the vicinity of the sapphire surface is limited, leading to reduced nucleation density. Additionally, under these conditions, the impact of viscous flow is minimal. This leads to the formation of molybdenum sulfide domains with uniform sizes across the entire wafer. When the gas flow rate increases to 140 sccm, the central region experiences a severe deficiency of Mo precursors due to rapid flow and limited residence time, causing non-equilibrium growth and the emergence of star-like triangular domain morphologies. Additionally, it was observed that when the gas flow rate reaches 100 sccm, the average size of the MoS_2 domains across the entire wafer exhibits

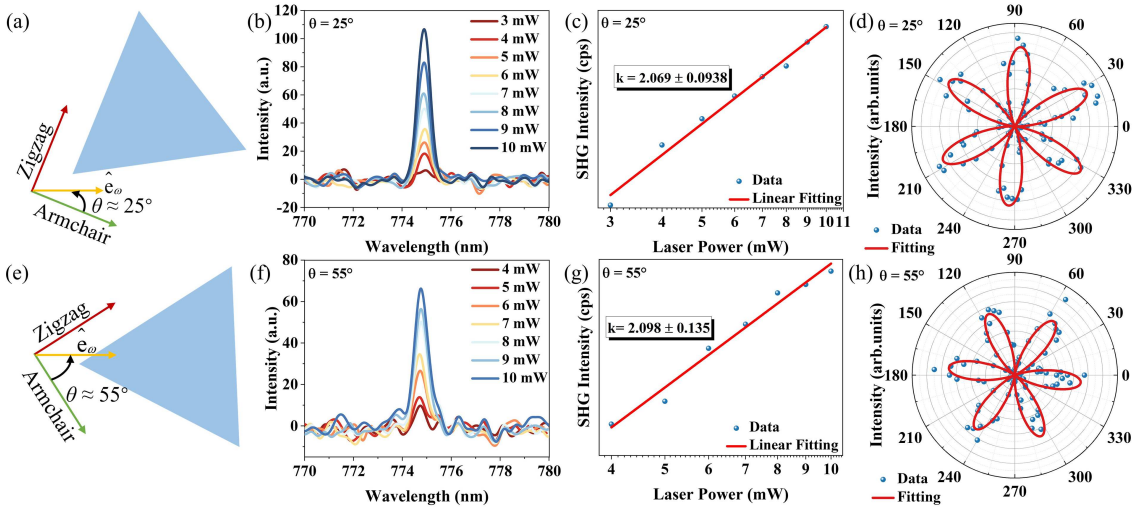

Figure 4 (Color online) (a) and (e) Schematics of incident laser direction and MoS_2 domain axes. θ is defined as the angle between the electric field direction of the incident light and the armchair direction of the sample. (b) and (f) Power-dependent SHG spectra of monolayer MoS_2 under 1550 nm laser excitation. (c) and (g) Log-log plots of SHG intensity as a function of excitation power, with linear fits shown in red. (d) and (h) Polarization-resolved SHG spectra for monolayer MoS_2 with different orientations. The SHG intensity follows the function $I = I_0 \sin^2(3\theta)$ under parallel polarization configuration, where I is the SHG intensity at angle θ and I_0 is the maximum SHG intensity. In this context, θ denotes the angle between the incident laser direction and the sample armchair direction [38]. The labeled values of $\theta = 25^\circ$ and $\theta = 55^\circ$ in the figure correspond to the angles between the incident laser direction and the armchair direction of the respective MoS_2 domains in panels (a) and (e).

a significant decrease with further increases in gas flow rate. This phenomenon is attributed to the excessively high gas flow rate, which reduces the residence time of the precursors near the substrate and leads to incomplete MoS_2 growth and smaller grain sizes. An optimal balance is achieved near 80 sccm, where the trade-off between precursor delivery and residence time results in favorable growth conditions, as shown in Figure S5. We performed a computational fluid dynamics (CFD) simulation to study the distribution of gas flow velocity in the CVD system, as shown in Figure S6. Through CFD simulations, we can clearly determine the gas velocity distribution within the tube furnace and the airflow distribution over the sapphire wafers, corresponding with the results discussed above. These results collectively indicate that carrier gas flow rate, in conjunction with wafer size, plays a decisive role in determining the growth dynamics and grain morphology of wafer-scale monolayer MoS_2 films synthesized by APCVD.

Due to the absence of in-plane inversion symmetry, monolayer MoS_2 exhibits pronounced second harmonic generation (SHG) [35–37]. As illustrated in Figures 4(a) and (e), two MoS_2 domains with distinct crystallographic orientations were randomly selected for SHG characterization. The incident excitation light was aligned at different angles relative to the armchair directions of the respective domains. Under 1550 nm laser excitation, a strong SHG signal with a peak at 775 nm was observed in both domains (Figures 4(b) and (f)), with intensity scaling as a function of pump power-indicative of high crystallinity and efficient nonlinear optical response. At the same time, Figures 4(c) and (g) present the log-log plots of SHG intensity versus excitation power, revealing a near-quadratic dependence with a slope of 2.0. This confirms that the MoS_2 obtained through APCVD exhibits good structural integrity and optical uniformity under pump light illumination, with no observable signs of photo-induced damage. The polarization-resolved SHG spectra (Figures 4(d) and (h)) exhibit the characteristic six-lobed pattern of 2H-phase MoS_2, with each lobe corresponding to a specific arm-chair crystal orientation in the sample. The polarization-dependent SHG response curves exhibit distinct variations across MoS_2 domains with different crystallographic orientations. This hexagonal rotational symmetry also aligns with the D_{3h} point group structure [35, 38]. These findings demonstrated that the synthesized monolayer MoS_2 exhibits a strong and tunable nonlinear optical response. This work not only confirms the excellent nonlinear optical properties of MoS_2 but also highlights its potential for use in next-generation optoelectronic and photonic applications involving 2D materials.

The electrical performance of wafer-scale MoS_2 was validated through FeFETs devices incorporating P(VDF-TrFE) as the ferroelectric dielectric layer. Figures 5(a) and (d) present the schematic and optical microscope image of the fabricated device, respectively. Details of the P(VDF-TrFE) preparation method are provided in Section 4. To confirm the ferroelectric properties of P(VDF-TrFE), P(VDF-TrFE) ferro-

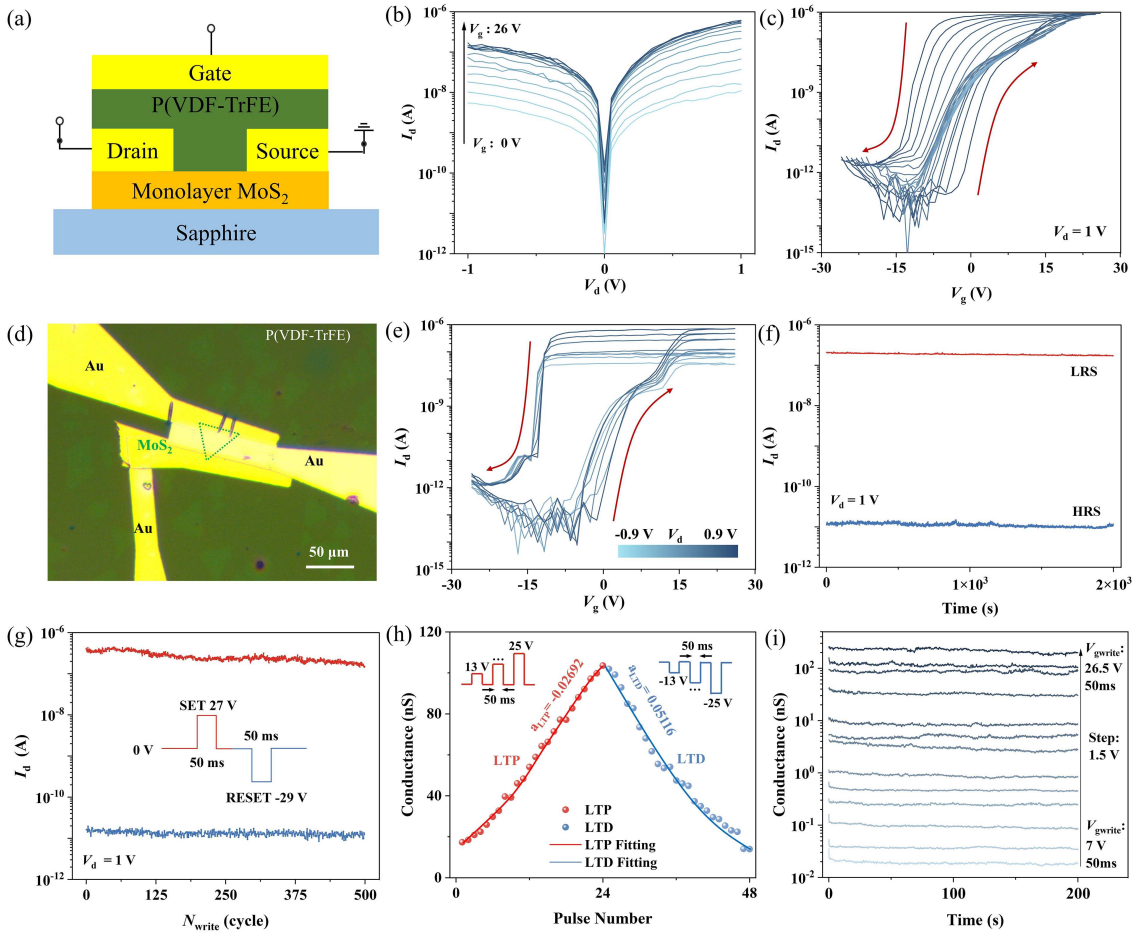

Figure 5 (Color online) (a) Schematic illustration of the FeFET structure, composed of a P(VDF-TrFE) ferroelectric dielectric layer and a monolayer MoS_2 channel. (b) Output characteristics of the monolayer MoS_2-based FeFET under varying gate (V_g). Transfer curves of the monolayer MoS_2-based FeFET measured with different V_g (c) and V_d (e). (d) Optical image of assembled monolayer MoS_2 FeFET. (f) Retention performance of FeFET in the high-resistance state (HRS) and low-resistance state (LRS). (g) Endurance test showing reversible resistance switching over 500 cycles; each gate voltage (V_g) pulse is 50 ms in duration and separated by a 0.2 s interval. The read voltage for the drain current is 1 V. (h) Evolution of conductance states as a function of the number of voltage pulses applied to FeFET, mimicking the LTP/LTD processes. Fitted LTP and LTD curves yield α values of -0.02692 and 0.05116, respectively. (i) Demonstration of multiple non-volatile conductance states in the MoS_2-based FeFET.

electric dielectric films were fabricated on gold-coated silicon wafers under identical processing parameters. Subsequently, writing, switching, and reading operations on ferroelectric domains were performed using PFM probes in piezoelectric force microscopy (PFM). Distinct domain boundaries in the amplitude images and contrast variations in the phase images confirm successful domain writing and switching, with polarity reversal achieved by applying a ± 27 V bias, as illustrated in Figures S6(b)–(d). Notably, the film thickness, measured by atomic force microscopy (AFM), is approximately 330.7 nm (Figure S7(a)), with thicker edges resulting from intentional scratches introduced from tweezers during sample preparation. The relative permittivity of P(VDF-TrFE) is 5 [39].

Figure 5(b) shows the output characteristics of the MoS_2-FeFET under various gate voltages V_g. The conductivity of the MoS_2 channel is modulated by the electrostatic doping effect of the ferroelectric P(VDF-TrFE) film, which results in an increase in output current. The output curves exhibit a clear symmetric conduction state, indicating a stable, linear response of MoS_2 to gate voltage and a uniformly conductive channel. When V_g reaches 26 V, the device achieves an on/off current ratio exceeding 10^6. Figures 5(c) and (e) show the respective transfer curves of the MoS_2-FeFET under different V_g and V_d scanning ranges, and Figure S8 shows the transfer characteristics curve incorporating leakage current. The curves exhibit a stable counterclockwise hysteresis with an expanding memory window (MW) at higher voltages, indicating that the carrier concentration in the MoS_2 channel is effectively controlled by ferroelectric polarization.

As shown in Figure 5(f), by reversing the polarization states of P(VDF-TrFE) between the upward and downward directions, the monolayer MoS_2-FeFET demonstrates clear switching behavior between low-resistance (LRS) and high-resistance (HRS) states, with a switching ratio exceeding 10^5. Figure 5(g) shows the endurance characteristics of the FeFET as a function of the switching cycles, with the figure inset displaying the voltage pulsing scheme used for the endurance examination. Under voltage pulse switching up to 500 cycles, MoS_2 FeFET shows almost no degradation in conductance switching properties, indicating a robust non-volatile memory writing capability [39, 40]. To verify the stability of the MoS_2-FeFET as a synaptic device, long-term potentiation (LTP) and long-term depression (LTD) measurements were taken across 24 discrete conductance states within the 1–100 nS range Figure 5(h). The obtained LTP/LTD cycles exhibited negligible cycle-to-cycle variability, indicating excellent stability and repeatability. By applying gate pulses to modulate the distribution of ferroelectric domains in the P(VDF-TrFE) dielectric layer, thus tuning the channel doping for multi-bit storage, the device achieves multi-level conductance states (Figure 5(i)), validating its potential for multi-bit memory and analog neuromorphic computing. Moreover, we compared our results with the performance of field-effect transistors fabricated from wafer-scale MoS_2 films prepared using existing LPCVD/MOCVD methods. As demonstrated in Table S1, the APCVD approach achieves a substantial on/off current ratio despite its lower cost. This establishes a solid foundation for its industrial implementation and demonstrates significant techno-economic advantages, particularly in semiconductor manufacturing applications requiring high switching ratios and low-cost producibility. In summary, wafer-scale monolayer MoS_2 films fabricated via APCVD exhibit excellent and uniform electrical performance in FeFET applications, demonstrating their suitability for future memory and neuromorphic device technologies.

3 Conclusion

In conclusion, we developed a multitube APCVD setup and used S and MoO_3 powders as precursors for fabricating high-quality wafer-scale monolayer MoS_2 films on vertical 2-inch sapphire substrates. Comprehensive characterization approaches confirmed that the grown monolayer MoS_2 films had high uniformity and high-quality crystal structure. The effect of the viscous flow of the carrier gas inside the quartz tube on crystal quality was investigated using the Knudsen equation. SHG results demonstrated the nonlinear optical properties of MoS_2 and confirmed its excellent crystal quality. Monolayer-MoS_2-based FeFETs were assembled, which exhibited an outstanding current modulation ratio exceeding 10^6 and reliable electrical characteristics. This study offers an effective and convenient solution to advance the standardization of research on 2D materials, establishing a solid foundation for fabricating large-scale MoS_2-based integrated circuits and flexible electronics.

4 Method section

4.1 Synthesis of wafer scale MoS_2

S (99.999%; Sigma-Aldrich) and MoO_3 (99.998%; Sigma-Aldrich) powders were used as precursors and placed in furnace tubes corresponding to the low-temperature zone (∼140°C) and medium-temperature zone (∼580°C), respectively. Single-side-polished sapphire substrates with C-plane orientation were selected and placed in the high-temperature zone (930°C), ∼20 cm away from the MoO_3 precursor. To ensure an atomically flat and clean substrate, sapphire was annealed at 1000°C under atmospheric pressure for 3 h under Ar and O_2 gas flows of 200 and 20 sccm, respectively, before the MoS_2 films were grown. The low-, medium-, and high-temperature zones were heated to their target temperatures for 50 min; subsequently, these temperatures were maintained for 40 min. The central miniature quartz tube contained 0.5 g of MoO_3, and the carrier-gas flow rate (Ar) was varied between 40 and 100 sccm. The outer quartz tubes were loaded with 10 g of the S powder, and Ar was made to flow through them at a rate of 100 sccm. After the growth process of the films, the furnace tubes were allowed to cool naturally to room temperature.

4.2 Device fabrication

The grown monolayer MoS_2 was used as the transistor channel, and gold stripes were transferred onto it for use as the source and drain electrodes by a standard dry transfer method using a position-precise transfer

system (Shanghai Onway). The P(VDF-TrFE) was spin-coated onto the MoS_2/sapphire substrate at 3000 r/min, followed by baking in an oven at 115°C for 15 min. This spin-coating and baking cycle was repeated three times, and subsequently vacuum-annealed at 135°C for 6 h. Subsequently, gold stripes were transferred onto the P(VDF-TrFE) dielectric layer as the top gate electrode using the standard dry transfer method.

4.3 Characterization

Raman spectra were acquired using a WITec Alpha 300 R using a 532 nm laser (8 mW) and an 1800 g/mm grating. Photoluminescence (PL) spectra were measured with the same laser at a power intensity of 1 mW, employing a 150 g/mm grating. X-ray photoelectron spectroscopy (XPS) measurements were conducted using a Thermo Scientific K-Alpha+ (ThermoFisher, USA) instrument, with binding energies calibrated using the C 1s peak at 284.6 eV. AFM images were obtained with an OXFORD Cypher ES instrument. SHG measurements were performed using a home-built vertical microscope setup in reflection geometry. All electrical measurements were conducted using an FS-Pro semiconductor parameter analyser and a micromanipulated probe station.

Acknowledgements This work was supported by National Natural Science Foundation of China (Grant Nos. 52202186, 62304069, 62025402, 62090033, 91964202, 92064003, 92264202, 62293522, 12104352, 12204294), China National Postdoctoral Programme for Innovative Talents (Grant No. BX20230281), Major Program of Zhejiang Natural Science Foundation (Grant No. DT23F0402), Xidian University Specially Funded Project for Interdisciplinary Exploration (Grant No. TZJH2024064), and China Postdoctoral Science Foundation (Grant No. 2024M752520).

Supporting information Figures S1–S8 and Table S1. The supporting information is available online at info.scichina.com and link.springer.com. The supporting materials are published as submitted, without typesetting or editing. The responsibility for scientific accuracy and content remains entirely with the authors.

References

1 Wang S, Liu X, Xu M, et al. Two-dimensional devices and integration towards the silicon lines. Nat Mater, 2022, 21: 1225–1239
2 Liu Y, Duan X, Shin H J, et al. Promises and prospects of two-dimensional transistors. Nature, 2021, 591: 43–53
3 Sun X, Zhu C, Yi J, et al. Reconfigurable logic-in-memory architectures based on a two-dimensional van der Waals heterostructure device. Nat Electron, 2022, 5: 752–760
4 Li D, Chen M, Sun Z, et al. Two-dimensional non-volatile programmable p-n junctions. Nat Nanotech, 2017, 12: 901–906
5 Jeong J W, Choi Y E, Kim W S, et al. Tunnelling-based ternary metal-oxide-semiconductor technology. Nat Electron, 2019, 2: 307–312
6 Novoselov K S, Mishchenko A, Carvalho A, et al. 2D materials and van der Waals heterostructures. Science, 2016, 353: aac9439
7 Akinwande D, Huyghebaert C, Wang C H, et al. Graphene and two-dimensional materials for silicon technology. Nature, 2019, 573: 507–518
8 Radisavljevic B, Radenovic A, Brivio J, et al. Single-layer MoS_2 transistors. Nat Nanotech, 2011, 6: 147–150
9 Qiu H, Yu Z H, Zhao T G, et al. Two-dimensional materials for future information technology: status and prospects. Sci China Inf Sci, 2024, 67: 160400
10 Peng Z R, Lin R F, Li Z, et al. Two-dimensional materials-based integrated hardware. Sci China Inf Sci, 2023, 66: 160401
11 Wang Z H, Xu B, Pei S H, et al. Recent progress in 2D van der Waals heterostructures: fabrication, properties, and applications. Sci China Inf Sci, 2022, 65: 211401
12 Withers F, Pozo-Zamudio O D, Mishchenko A, et al. Light-emitting diodes by band-structure engineering in van der Waals heterostructures. Nat Mater, 2015, 14: 301–306
13 Singh S, Modak A, Pant K K, et al. MoS_2-nanosheets-based catalysts for photocatalytic CO_2 reduction: a review. ACS Appl Nano Mater, 2021, 4: 8644–8667
14 Shanmugam M, Bansal T, Durcan C A, et al. Schottky-barrier solar cell based on layered semiconductor tungsten disulfide nanofilm. Appl Phys Lett, 2012, 101: 263902
15 Lin Z, Liu Y, Halim U, et al. Solution-processable 2D semiconductors for high-performance large-area electronics. Nature, 2018, 562: 254–258
16 Guo Y H, Wang Y, Deng W J, et al. MoS_2 synaptic transistor with one-step manufacture. Sci China Inf Sci, 2025, 68: 112401
17 Kumar R, Goel N, Kumar M. UV-activated MoS_2 based fast and reversible NO_2 sensor at room temperature. ACS Sens, 2017, 2: 1744–1752
18 Splendiani A, Sun L, Zhang Y, et al. Emerging photoluminescence in monolayer MoS_2. Nano Lett, 2010, 10: 1271–1275
19 Li T, Guo W, Ma L, et al. Epitaxial growth of wafer-scale molybdenum disulfide semiconductor single crystals on sapphire. Nat Nanotechnol, 2021, 16: 1201–1207
20 Yu H, Liao M, Zhao W, et al. Wafer-scale growth and transfer of highly-oriented monolayer MoS_2 continuous films. ACS Nano, 2017, 11: 12001–12007
21 Wang Q, Li N, Tang J, et al. Wafer-scale highly oriented monolayer MoS_2 with large domain sizes. Nano Lett, 2020, 20: 7193–7199
22 Liu L, Li T, Ma L, et al. Uniform nucleation and epitaxy of bilayer molybdenum disulfide on sapphire. Nature, 2022, 605: 69–75
23 Zhu J, Park J H, Vitale S A, et al. Low-thermal-budget synthesis of monolayer molybdenum disulfide for silicon back-end-of-line integration on a 200 mm platform. Nat Nanotechnol, 2023, 18: 456–463
24 Valdivia A, Tweet D J, Conley J J F. Atomic layer deposition of two dimensional MoS_2 on 150 mm substrates. J Vacuum Sci Tech A-Vacuum Surfs Films, 2016, 34: 021515
25 Jurca T, Moody M J, Henning A, et al. Low-temperature atomic layer deposition of MoS_2 films. Angew Chem Int Ed, 2017, 56: 4991–4995

26 Li X L, Li Y D. Formation of MoS_2 inorganic fullerenes (IFs) by the reaction of MoO_3 nanobelts and S. Chem Eur J, 2003, 9: 2726–2731
27 Lee C, Yan H, Brus L E, et al. Anomalous lattice vibrations of single- and few-layer MoS_2. ACS Nano, 2010, 4: 2695–2700
28 Xia Y, Chen X, Wei J, et al. 12-inch growth of uniform MoS_2 monolayer for integrated circuit manufacture. Nat Mater, 2023, 22: 1324–1331
29 Mao J, He J, Io W F, et al. Strain-engineered ferroelectricity in 2H bilayer MoS_2. ACS Nano, 2024, 18: 30360–30367
30 Liang J, Zou Z, Liang J, et al. Layer-by-layer epitaxy growth of thickness-controllable two-dimensional tungsten disulfide. Sci China Inform Sci, 2024, 67: 1-9
31 Wang J, Cai X, Shi R, et al. Twin defect derived growth of atomically thin MoS_2 dendrites. ACS Nano, 2018, 12: 635–643
32 Xu J, Srolovitz D J, Ho D. The adatom concentration profile: a paradigm for understanding two-dimensional MoS_2 morphological evolution in chemical vapor deposition growth. ACS Nano, 2021, 15: 6839–6848
33 Xu W, Li S, Zhou S, et al. Large dendritic monolayer MoS_2 grown by atmospheric pressure chemical vapor deposition for electrocatalysis. ACS Appl Mater Interfaces, 2018, 10: 4630–4639
34 Livesey R G. Flow of gases through tubes and orifices. In: Foundations of Vacuum Science and Technology. Hoboken: John Wiley & Sons, Inc., 1998. 81–140
35 Kumar N, Najmaei S, Cui Q, et al. Second harmonic microscopy of monolayer MoS_2. Phys Rev B, 2013, 87: 161403
36 Zeng H, Liu G B, Dai J, et al. Optical signature of symmetry variations and spin-valley coupling in atomically thin tungsten dichalcogenides. Sci Rep, 2013, 3: 1608
37 Liang J, Zhang J, Li Z, et al. Monitoring local strain vector in atomic-layered $MoSe_2$ by second-harmonic generation. Nano Lett, 2017, 17: 7539–7543
38 Dang Z, Guo F, Duan H, et al. Black phosphorus/ferroelectric P(VDF-TrFE) field-effect transistors with high mobility for energy-efficient artificial synapse in high-accuracy neuromorphic computing. Nano Lett, 2023, 23: 6752–6759
39 Feng G, Zhu Q, Liu X, et al. A ferroelectric fin diode for robust non-volatile memory. Nat Commun, 2024, 15: 513
40 Bian R, He R, Pan E, et al. Developing fatigue-resistant ferroelectrics using interlayer sliding switching. Science, 2024, 385: 57–62